IFASD 2015
International Forum on Aeroelasticity and Structural Dynamics
June 28 — July 02, 2015 ▲ Saint Petersburg, Russia

Wind Tunnel Test of a Morphing Wingtip Leading Edge

R C M Cheung[1], C Wales[1], J E Cooper[1], S Vasista[2], J Riemenschneider[2], B van de Kamp[2], H P Monner[2]

[1]Department of Aerospace Engineering, University of Bristol, UK.

j.e.cooper@bristol.ac.uk

[2]Institute of Composite Structures and Adaptive Systems, German Aerospace Center (DLR), Braunschweig, Germany

Keywords: morphing wing, droop-nose, compliant mechanism

Abstract: A full scale morphing wing tip demonstrator with a droop-nose adaptive morphing wingtip was wind tunnel tested as part of the European FP7 project NOVEMOR. This demonstrator features a flexible fiberglass skin and internal superelastic nickel titanium and aluminium compliant mechanisms. The tests were carried out to assess the performance of the skin and compliant mechanisms under aerodynamic loading; the wing performed as it was designed to. The results show that strains in the mechanism are mainly due to the actuation showing the adequate stiffness of the mechanism. In addition to strains, pressure data was taken to determine aerodynamic loading. Finite element and computational fluid dynamics simulations performed and overall show good agreement with the experimental values.

1 INTRODUCTION

There is a considerable drive via initiatives such as FlightPath 2050 [1] and Clean Sky to develop environmentally friendly aircraft. Consideration of the Breguet range equation shows that in order to improve the range one can either: i. improve the aerodynamics (L/D), ii. reduce the structural weight, or iii. incorporate better engines (SFC); this work aims to address the first two approaches. Morphing technologies provide one approach to improve the aerodynamic performance throughout the flight envelope by changing the aerofoil shape [2]; the development of a capability to achieve a drooping leading edge is one such technology that has great promise [3, 4].

NOVEMOR (Novel Air Vehicle Configurations: from Fluttering Wings to Morphing Flight) is a FP7 project aiming to investigate novel configurations and morphing wing solutions to enable environmentally friendly and cost-effective air transportation. This paper presents research conducted in the European FP7 project NOVEMOR, in which an adaptive morphing wingtip (AMWT) of the form of a leading-edge droop-nose morphing device is wind tunnel tested. The leading edge of the AMWT, designed and manufactured by the DLR, consists of a flexible composite skin with a tailored thickness distribution which droops smoothly based on input forces from actuators transmitted through internal mechanisms. The reference aircraft is a regional jetliner with geometry and aerodynamic data provided by project partner Embraer, as shown in Figure 1. The AMWT device was envisaged as a suitable candidate for drag reduction, as well as to overcome some aeroelastic problems that classical wing control surfaces can encounter such as aileron efficiency loss with increasing dynamic pressure. Furthermore, the wing lift distribution may be adjusted in flight by the AMWT to best suit the prevailing conditions, resulting in higher overall efficiency. One key feature of the AMWT is the use of compliant mechanisms to transfer the actuation force to the skin instead

of conventional rigid-link mechanisms, with the anticipated benefits including potential weight savings, reduced part and assembly costs, and the elimination of backlash.

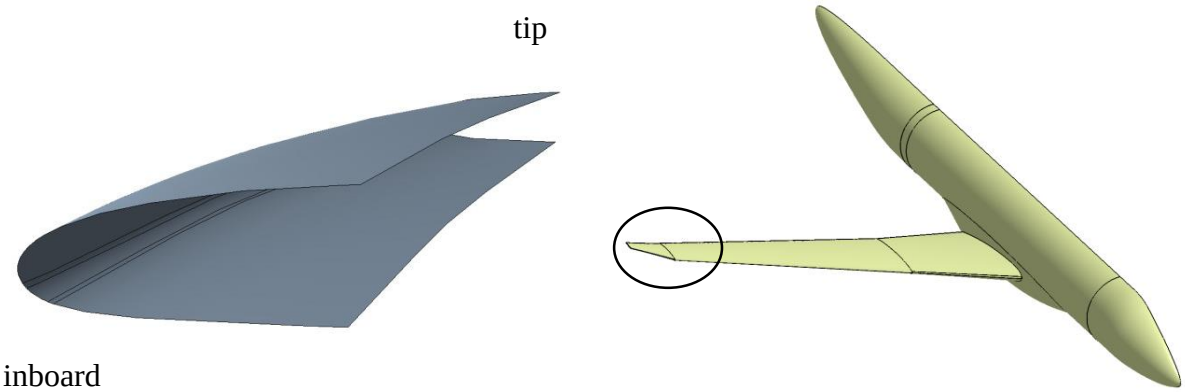

Figure 1. 3D geometry of aircraft and wingtip leading edge

This paper presents the results of wind tunnel test conducted on a full scale demonstrator of the AMWT. The model will be tested over a range of different tunnel speeds and angles of incidence. Objectives of the test are to demonstrate the functionality of the morphing LE device over a range of test conditions (up to 55 m/s) and assess the performance of the compliant mechanism under aerodynamic loading.

2 DESIGN

The morphing wingtip demonstrator is based on a full scale jetliner wingtip, with dimensions of 1.3m semi-span, 1.5m root chord, 0.6m tip chord and 45^0 leading edge sweep. The morphing region consists of the front third of the wingtip. The target morphed leading edge shape features an approximate droop angle of 2° from the clean shape.

One of the key requirements of a morphing wing device, in general, is that the outer profile of the structure should be able to assume multiple shapes under different actuation states and external (e.g. aerodynamic) loads with minimal deviation from the specified target profiles. This applies to the AMWT device where the leading edge profile of the wingtip needs to conform to the clean target shape without actuation input and the droop shape when actuated. The concept for the morphing leading edge is shown in Figure 2. The design consists of two compliant mechanisms each driven by a linear actuator. The compliant mechanism is connected to the stringer via a steel strips in order to distribute the force from the mechanism over a greater spanwise distance of the stringer. Actuating the motor results in a linear motion of the shaft which drives the compliant mechanism and droops the skin.

The skin was designed using a DLR design tool [5] based on a Simplex search optimisation method. The optimiser was used to determine the ply drop-offs and the individual ply orientations. The final design has between 8 and 32 plies of Hexcel HexPly913® prepreg plies. The final skin had a symmetric ply stacking sequence using 0°, ±45° and 90° ply angles. The ply drop offs were made in made in the middle layers so that the inner and outer four plies cover the entire surface. The 0° layer was positioned 38° from the flight direction to avoid the occurrence of helicals as the plies wrap around the curved leading edge.

The compliant mechanism was designed using a topology optimization approach. The aim of the optimisation was essentially to maximise the stiffness of the mechanism whilst subject to displacement constraints such that the mechanism moved to its target points and a volume constraint. This means that the mechanism is a structure designed to have high stiffness which moves to a precise location under specific boundary conditions. In order to facilitate this movement without compromising the structural integrity, a material with high yield capacity was required i.e. the superelastic nickel titanium. Further details of the compliant mechanism design can be found in [4] and the final compliant mechanisms can be seen in Figure 2.

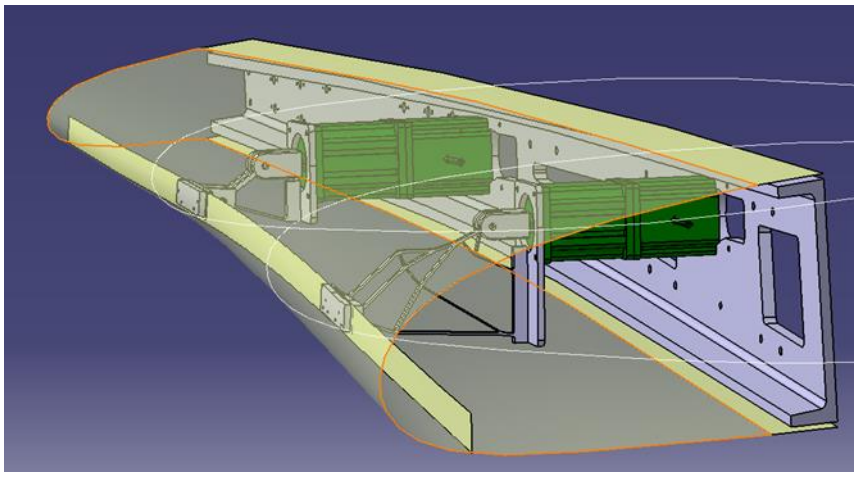

Figure 2 Conceptual drawing of the DLR droop-nose device.

3 MANUFACTURE

The wind tunnel model was manufactured in two main sections. The front third of the wing tip is the morphing leading edge which makes the first main piece and the rear rigid two thirds was manufactured as the second main piece. The droop-nose leading edge comprises a number of components, including a composite GFRP skin, auxiliary aluminium spar, compliant mechanisms and actuators. The second piece comprises a machined polyurethane skin over a steal frame.

Due to the 3D geometrical complexity and the need for an integral stringer, to connect to the compliant mechanism, the skin was manufactured in two curing stages. In the first stage, all the layers in the first half of the mould were taken up to stringer (with some tapering to allow lapping with the part of the second curing stage) and then cured. The remaining half was then laid-up up to the first cured stringer and then cured. The result was a seamless and continuous skin and an integral stringer.

The inboard compliant mechanism (superelastic nickel titanium) was fabricated using wire EDM. The outboard compliant mechanism assembly and the actuator mounts were manufactured by laser cutting a single stock sheet of aluminium 7075.

Electrical off-the-shelf captive linear stepper motor actuators were used to drive the compliant mechanisms and the skin. Due to high forces (>1500 N) and low speeds required (<5 mm/s) actuators with a small lead (1.27 mm) were chosen. Two actuators of the same type were used, one for each actuator. External displacement sensors were installed in an open-loop configuration to provide the user the current position information of the actuator. Whilst programming of the motors was achieved by specifying a number of steps to deliver the desired actuation stroke, the external displacement sensors were installed in the event that the motor loses steps due to higher than expects loads.

4 INSTRUMENTATION

The primary interest of the test was investigating the structural performance of compliant mechanism under aerodynamic loading. As such the primary instrumentation consisted of 14 bonded strain gauges, with all strain gauges being of quarter-bridge configuration, to measure the total strain (i.e. combined axial and bending strain). The strain gauge signals were first amplified by a calibrated amplifier before being captured by LMS data acquisition hardware and the LMS test.Xpress measurement software. External displacement sensors were installed to monitor actuator strokes and video cameras were mounted inside the leading edge for visual inspection. Figure 3 shows the wingtip in the wind tunnel with its instrumentation.

In addition to the strain measurements, the total loads and pressures were measured to obtain the air loads acting on the droop leading edge. A total of 63 pressure tappings were installed in the wingtip, with 39 installed in the droop-nose leading edge region with a uniform spacing of approximately 20 mm and 22 installed in the wingbox/trailing edge region. The pressure tappings were installed 0.555m from the root plane, lying in-between the two mechanism stations. The pressure tappings were aligned in the flight direction.

5 WIND TUNNEL TEST MATRIX

The wind tunnel test matrix involved running three different droop configurations (0%, 50% and 100% droop) through angles of attack (AoAs) ranging from -10° to +10° at 2.5° increments and wind tunnel test speeds from 25 to 55 m/s at 5 m/s increments. The test matrix needed not be fixed but could evolve based on the behaviour of the AMWT at lower speeds/angles of attack say.

Midway through the testing, an incident occurred where the actuators were accidently set to 200% of their maximum design stroke, resulting in some local plastic deformation of the inboard compliant mechanism. In order to maintain validity of the experiment, the results are presented in two sets: i) Set 1 – before plastic deformation and ii) Set 2 – after plastic deformation. In this way, the two sets can be compared and the effect of the plastic deformation on the behaviour can be analysed. The actual wind tunnel test matrix thus employed in the tests is also split into these two sets and are shown in Tables 1-3. In all cases other than those noted “Transient”, the measurements were made at steady state condition i.e. once the wind flow was steady. Data collected over these steady state runs were measured over 6 seconds and then averaged. Two transient cases were also conducted at a steady flow speed of 50 m/s and another transient with air-off, whereby the data was measured whilst the AMWT was drooping and un-drooping.

a)

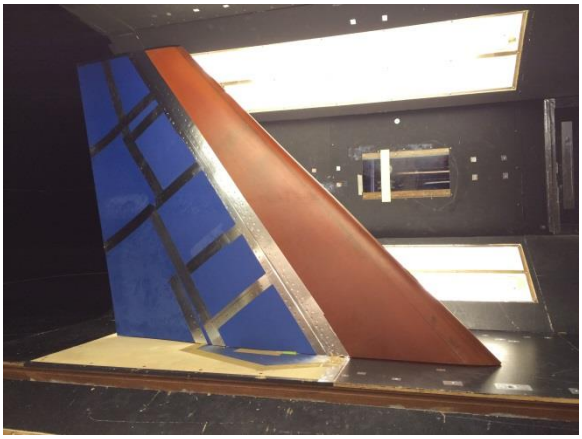

b)

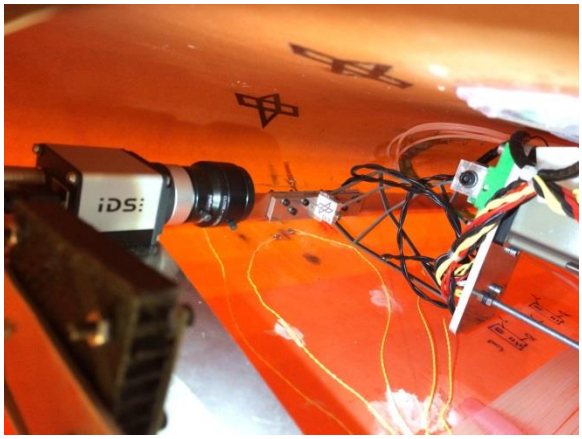

c)

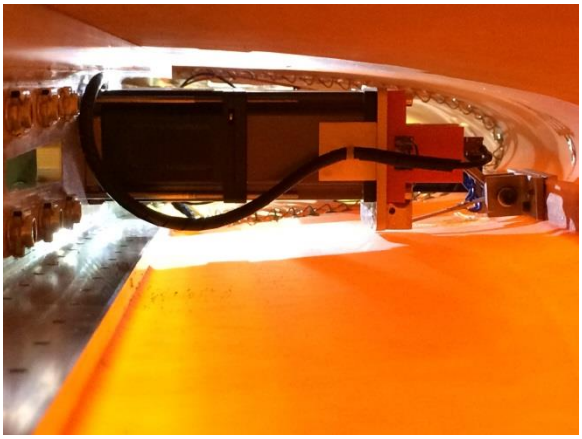

d)

Figure 3 Photos of a) and b) the droop-nose adaptive morphing wingtip mounted in the wind tunnel and c) and d) instrumentation used for the strain, pressure, actuator and visual measurements.

AoA, °	-2.5	0	+2.5	+5
Droop, %	0, 50, 100	0, 50, 100	0, 50, 100	100
Wind Speed, m/s	0, 25, 30, 35, 40, 45, 50, 55	0, 25, 30, 35, 40, 45, 50, 55	0, 25, 30, 35, 40, 45, 50, 55	0, 25, 30, 35, 40, 45, 50, 55

Table 1 Set 1 test matrix – before plastic deformation (steady state)

AoA, °	-10	-5	0	+5	+10
Droop, %	0, 50, 100	0, 50, 100	0, 50, 100	0, 50, 100	0, 50, 100
Wind Speed, m/s	0, 25, 30, 35, 40, 45, 50, 55	0, 25, 30, 35, 40, 45, 50, 55	0, 25, 30, 35, 40, 45, 50, 55	0, 25, 30, 35, 40, 45, 50, 55	0, 25, 30, 35, 40, 45, 50, 55

Table 2 Set 2 test matrix – after plastic deformation (steady state)

AoA, °	0	0	0
Droop, %	0 → 100 → 0	0 → 200 → 0	0 → 250 → 0
Wind Speed, m/s	50	50	0

Table 3 Transient test matrix – after plastic deformation

6 RESULTS

6.1 Ground Tests

Ground tests involved strain measurements at 100% droop and 3D ATOS surface scans of the droop-nose in the clean and 100% droop configurations. These ground tests results are available in [6] to which the reader is referred and so are omitted here. There was good agreement between the ground tests and finite element results for the skin and inboard compliant mechanism strains though the outboard mechanism results show less strain than expected. The strains in the skin were low (in the order of 0.09%) due to the small 2° droop deflection and the inboard compliant mechanism featured high strain (in excess of 2%) which the superelastic nickel titanium material can withstand safely.

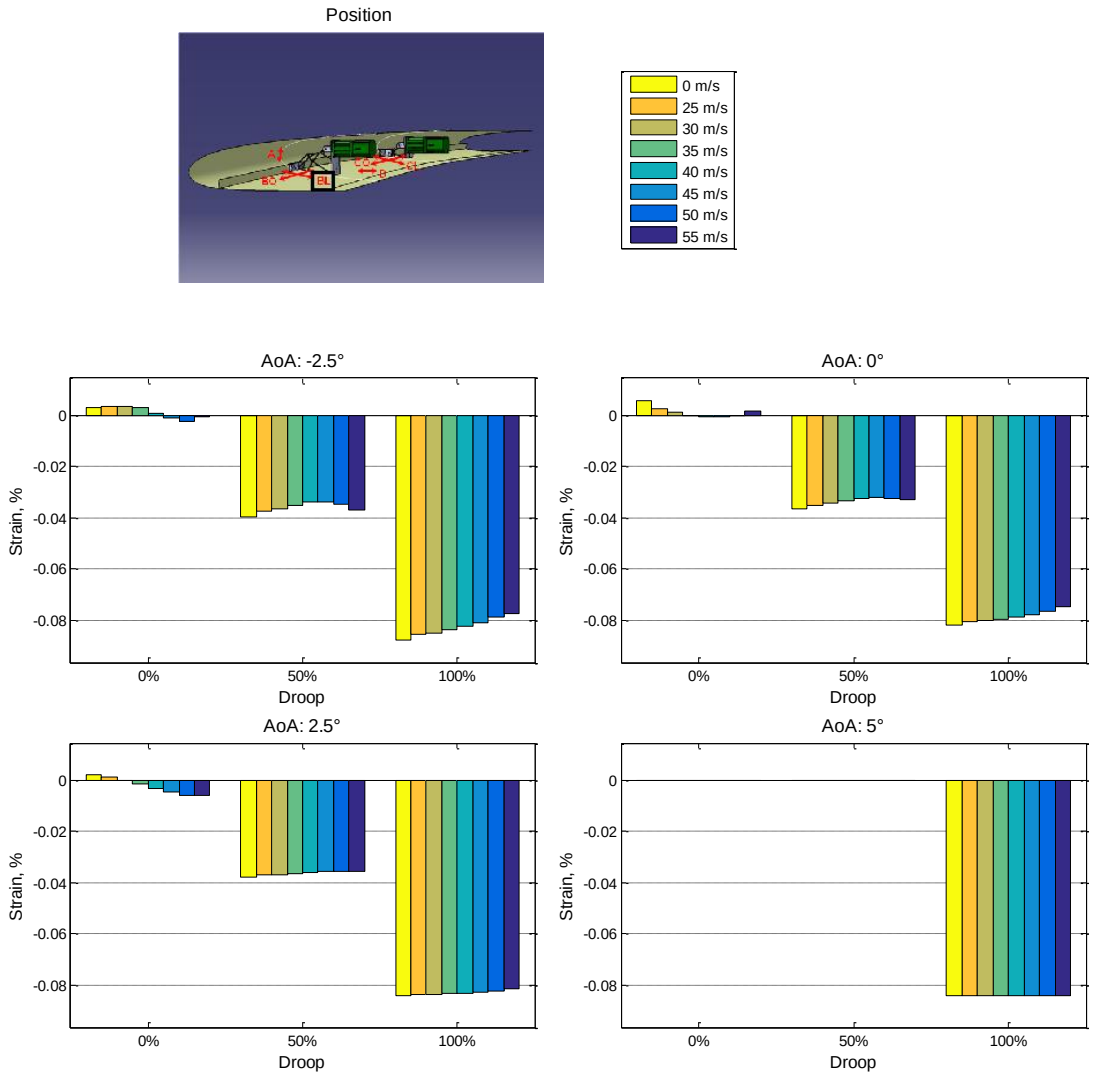

Figure 4 Set 1 measured strains for the skin position BL

6.2 Strains

The Set 1 results for skin strain gauge position BL are shown in Figure 4. This strain position was the highest amongst the skin strain gauges and it is clear that the strains are very low in

the order of 0.08% at 100% droop (i.e. 2° droop). It is also clear that change in strain due to the drooping action is significantly higher than any change due to the aerodynamic loads (with increasing flow speed or angle of attack).

The Set 1 strain results for the position IB1 are shown in Figure 5. The maximum strain is in the order of 2.1 % and the change in strain due to the aerodynamic loading is small. There is a slight relieving effect of the strain at 100 % droop.

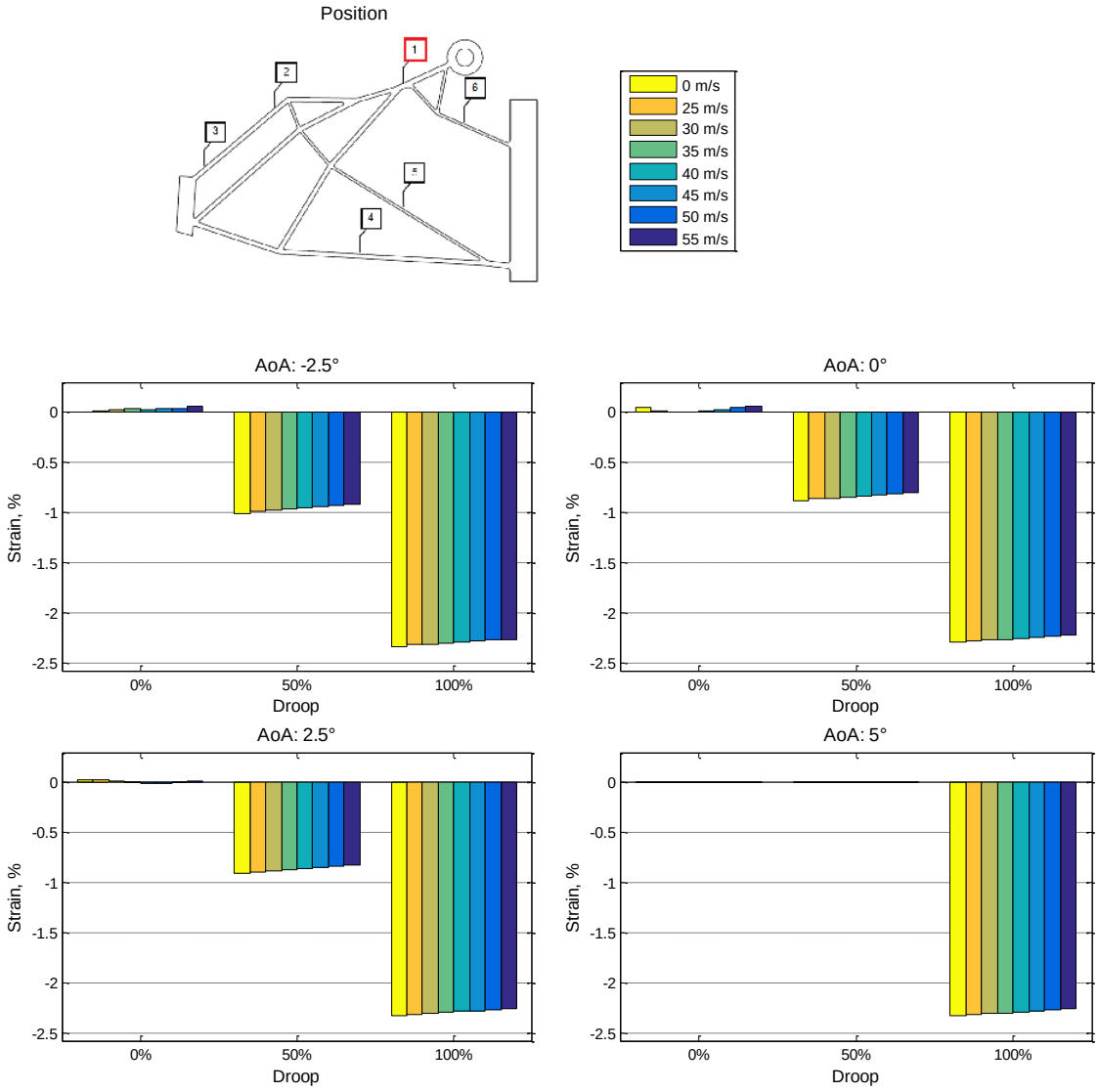

Figure 5 Set 1 measured strains for the inboard compliant mechanism position IB1

The Set 2 strain results for the position IB1 are shown in Figure 6 There is a small offset of strain in the order of 0.1% compared to the results of Set 1 in Figure 5 indicating that there is a small effect from the plastic deformation. It is difficult to identify whether the plastic strain occurred in the strain gauge or the material itself, but as a conservative approach it will be assumed that the plastic strain occurred in the mechanism material. A noticeable effect was noticed at -10° AoA where the change in strain was relatively high. This is especially noticeable for the results of strain position IB5 shown in Figure 7, with buckling clearly evident in Figure 8. At -10° AoA, the leading edge at the root was very close to the wind

tunnel wall, resulting in a highly localised and high suction peak. It can be seen that the strain is near-zero for all other angles of attack.

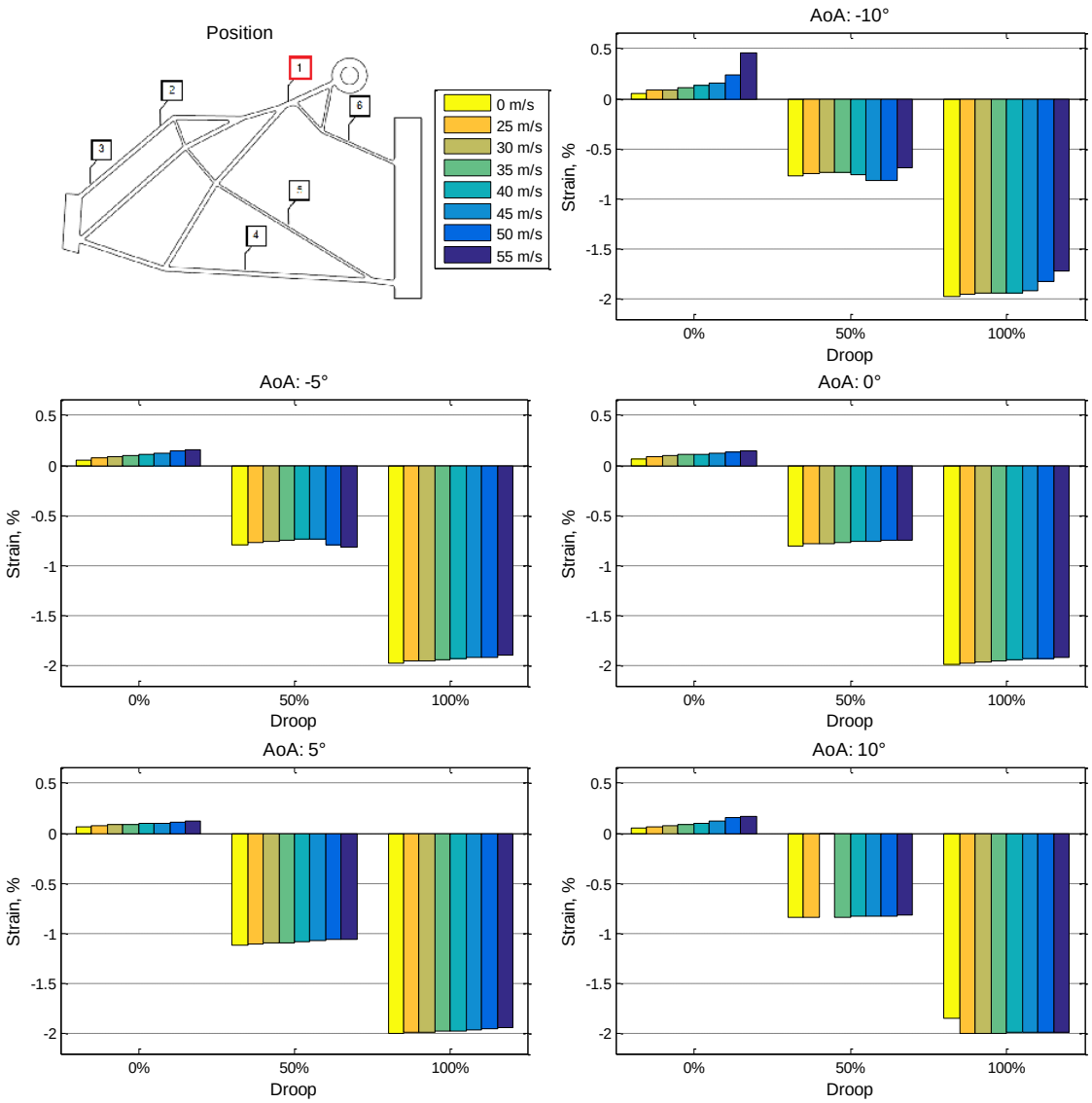

Figure 6 Set 2 measured strains for the inboard compliant mechanism position IB1.

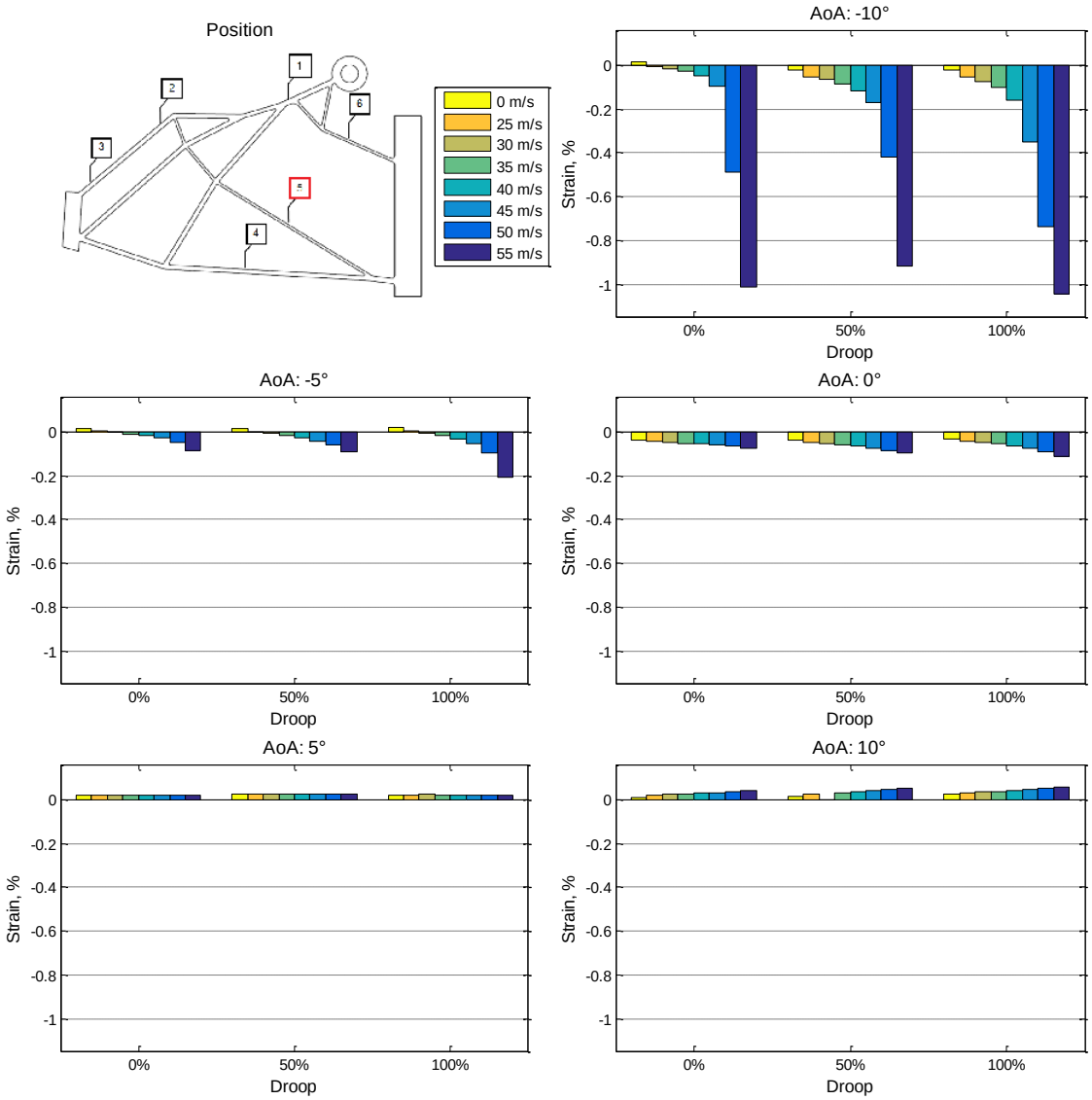

Figure 7 Set 2 measured strains for the inboard compliant mechanism position IB5.

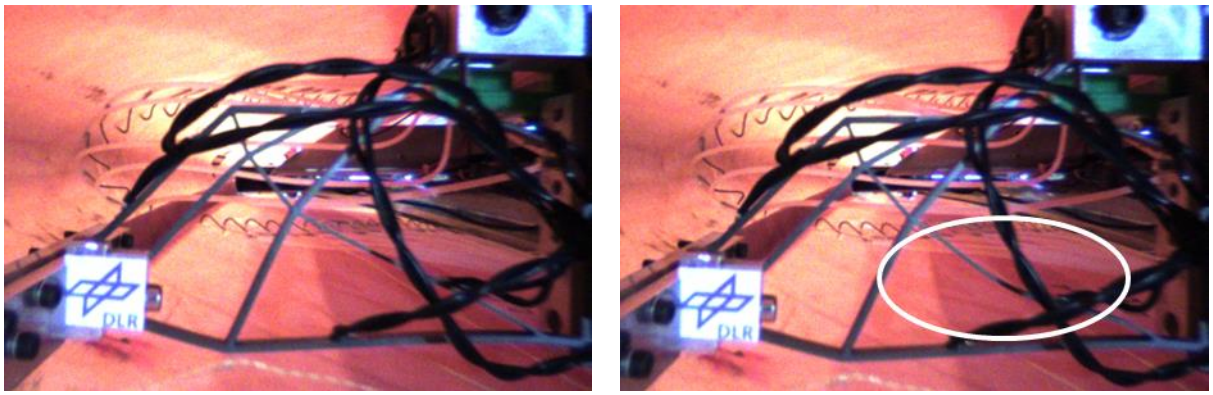

Figure 8 Photo of inboard compliant mechanism at -10° AoA and 100% droop. Left: Zero airflow; Right: buckling at position IB5 at 55 m/s wind tunnel flow speed.

The Set 2 strain results for the position OB8 are shown in Figure 9. The trends are similar to the other strain positions presented above. The magnitude is in the order of 0.15%, suggesting that there is allowance for further strain (0.7% yield limit for aluminium 7075)

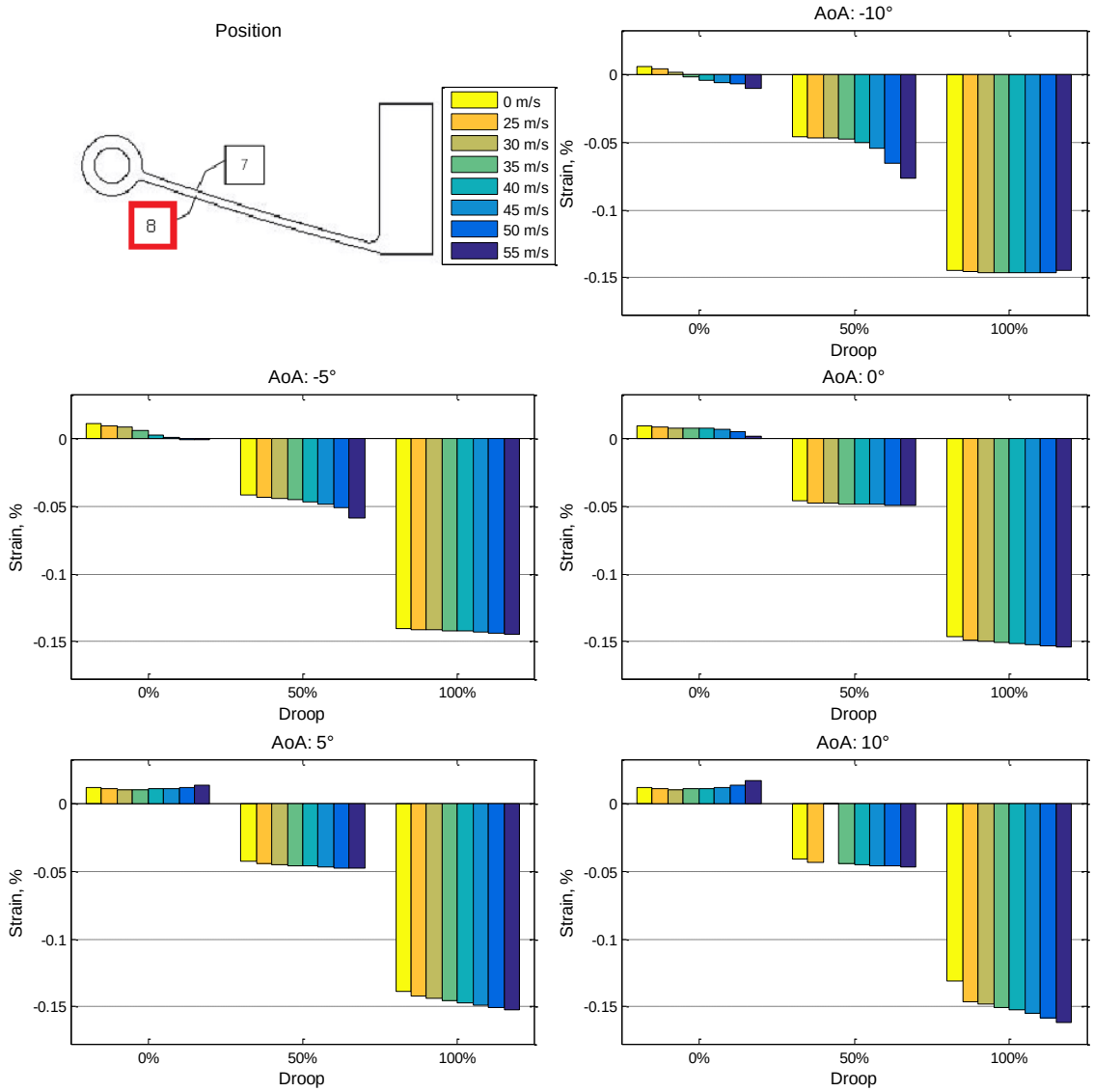

Figure 9 Set 2 measured strains for the outboard compliant mechanism position OB8.

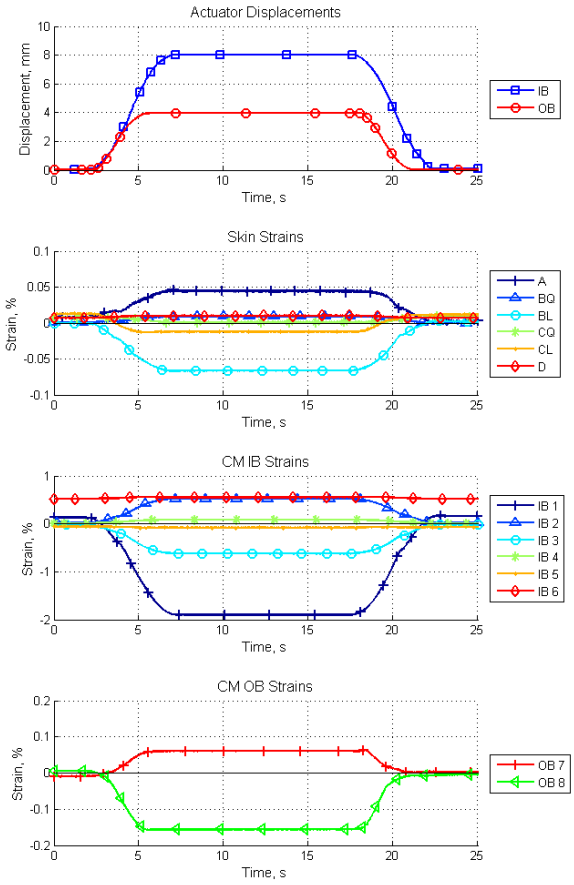

Figure 10 Measurements for transient run at 0° AoA, 50 m/s and droop cycle of 0% → 100% →0%.

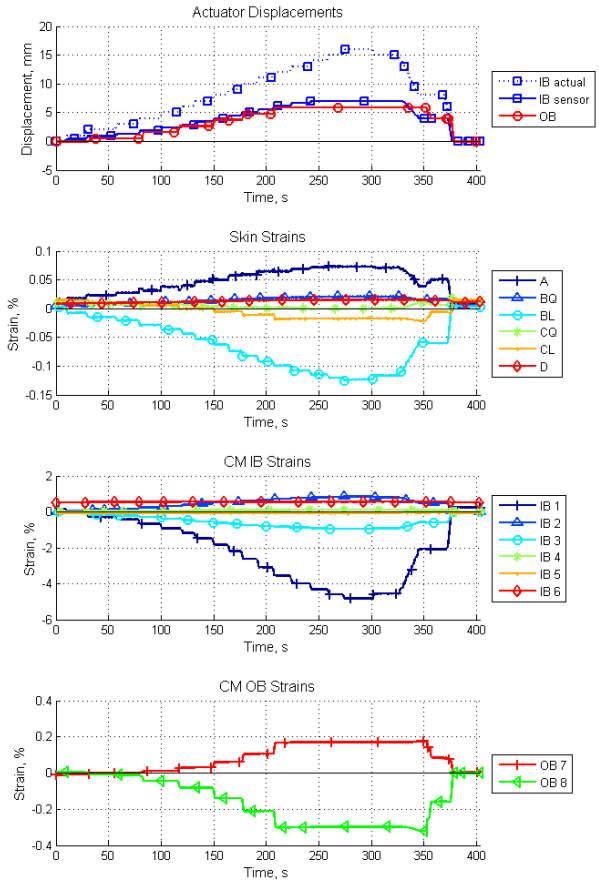

Figure 11 Measurements for transient run at 0° AoA, 50 m/s and droop cycle of 0% → 200% → 0%

The transient measurement results are shown in Figures 10-12. As final tests of the wind tunnel test regime, it was envisaged to push the inboard compliant mechanism up to failure and hence cases of 200% and 250% actuator stroke were run. The results are intuitive with the strains responding linearly with actuator input. For the 200% and 250% cases (Figures 11 and 12), the actuator stroke was increased incrementally and then returned to the zero position. There inboard actuator external displacement sensor channel was saturating for these cases hence the lower than actual displacement reading. However, the displacement was observed via the camera and confirmed visually. An interesting result can be seen in Figure 12 where shortly after the 200% actuator stroke mark (at approximately 116 seconds) the strains stop growing and change direction. This was due to a type of "snap-through" behaviour of the inboard mechanism around region IB6. This is evident in the sequence of photos in Figure 13. An important result was that the mechanism did not break at 250% actuator deflection, signifying the relevance of the superelastic material.

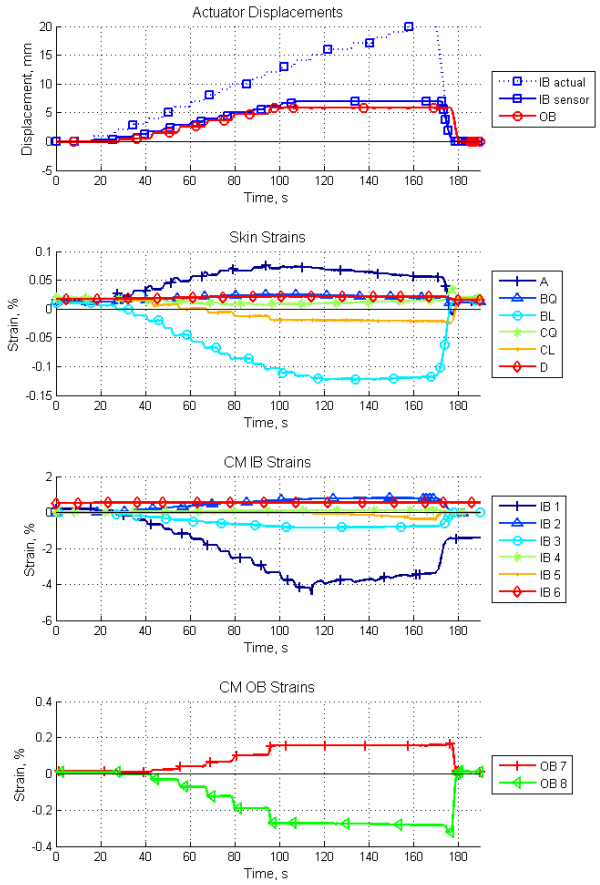

Figure 12 Measurements for transient run at 0° AoA, 0 m/s and droop cycle of 0% →250% → 0%.

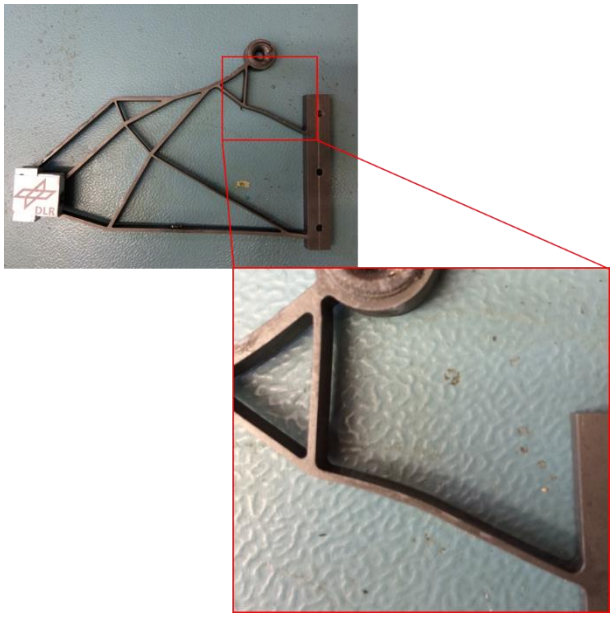

Figure 13 Inboard compliant mechanism after disassembly with zoomed in region of plastic deformation.

6.3 Pressures

CFD simulations were carried out using the Tau solver for the 0% and 100% droop cases to obtain the pressure field over the entire wind tip. The CFD simulation are compared to the pressures and total loads measured experimentally. The 0% droop case was meshed from the surface CAD geometry. For the 100% droop case the mesh was based on 3D scans of the deformed leading edge performed outside the tunnel. The region captured by the scanner is 5 mm from the inboard and 1 mm from the outboard. In constructing the CFD mesh the inboard surface is linearly extrapolated to tunnel wall. The outboard end was left 1mm shorter.

The CFD simulation was performed for the wing in the tunnel working section. The inflow condition was set as uniform flow at 55m/s. At the exit of the working section an Exit-pressure outflow condition was used. This was set up so that the pressure in the working section at the reference pressure point matches the measured experimental value. The simulations were performed using the Tau CFD [7, 8] solver with the Spalart Allmaras turbulence model [9].

Figure 14 shows the CFD results compared to the experimental data at 55m/s. The 0% droop cases generally show fairly good agreement with the experimental data. The 100% droop

cases do not show as good agreement with the experimental but match the trend in change in pressure coefficient due to droop. It can be seen that the CFD matches the trend in pressure change due to droop but over predicts the amount.

The results show that for angles of attack from -10° to 0° that increasing the droop increases the suction peak by a small amount. For 5° and 10° angles of attack the trend is reversed and increasing the droop leads to a reduction in the pressure coefficients. The pressure results are consistent with lift results shown in Figure 15. For negative angles of attack the magnitude of the lift increases with increasing levels of droop. For positive angles of attack the increasing the amount of droop decreases the lift achieved.

The high suction peak for the -10° case is explained by the leading edge being close to the wind tunnel wall at this angle of attack. The maximum C_p variation at 100% droop at -10° AoA is in the order of 0.16. This value was expected to be small given the small droop target of 2° as specified by Embraer.

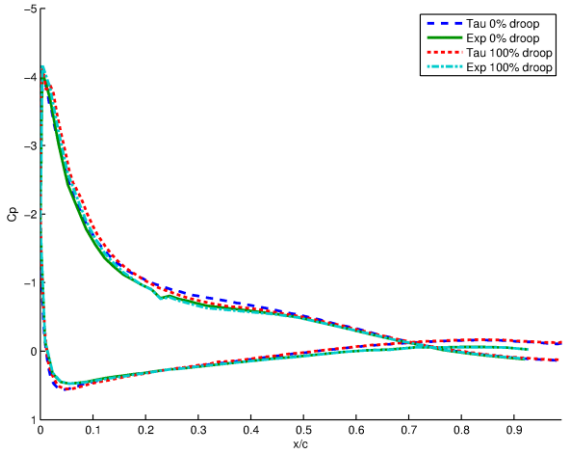

a) -10°

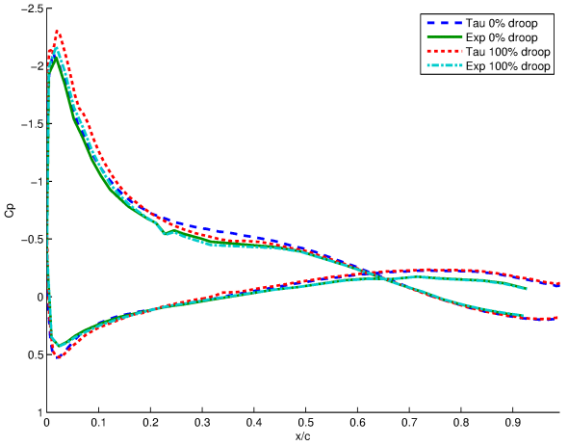

b) -5°

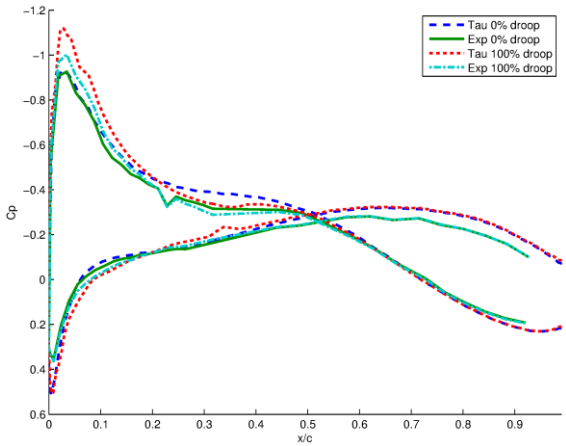

c) 0°

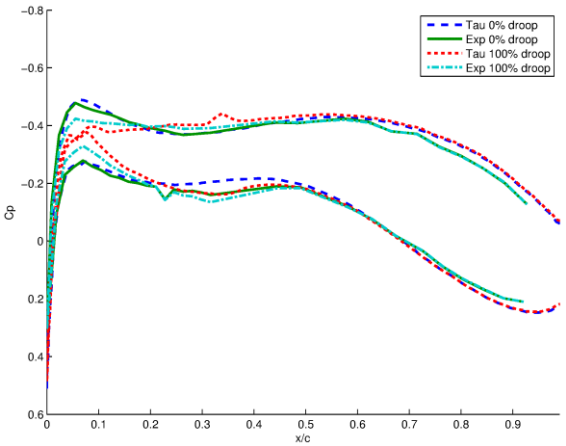

d) 5°

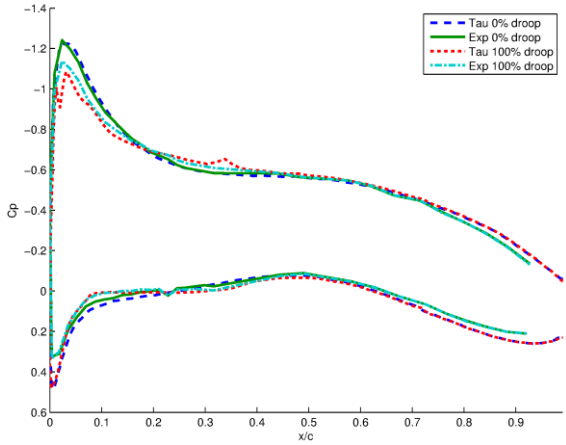

e) 10°

Figure 14 Comparison of CFD pressures with experimental values at 55m/s

To further validate CFD simulations the total lift was compared to the experimental lift, see Figure 15. The CFD results show a linear change in lift across the angle of attack range. This shows fairly good agreement with the measure lift between -5° to 0°. For angle of attack outside this range the CFD over predicts the magnitude of the lift. The CFD also generally predicts a much small change in lift from 0% to 100% droop compared to experiment.

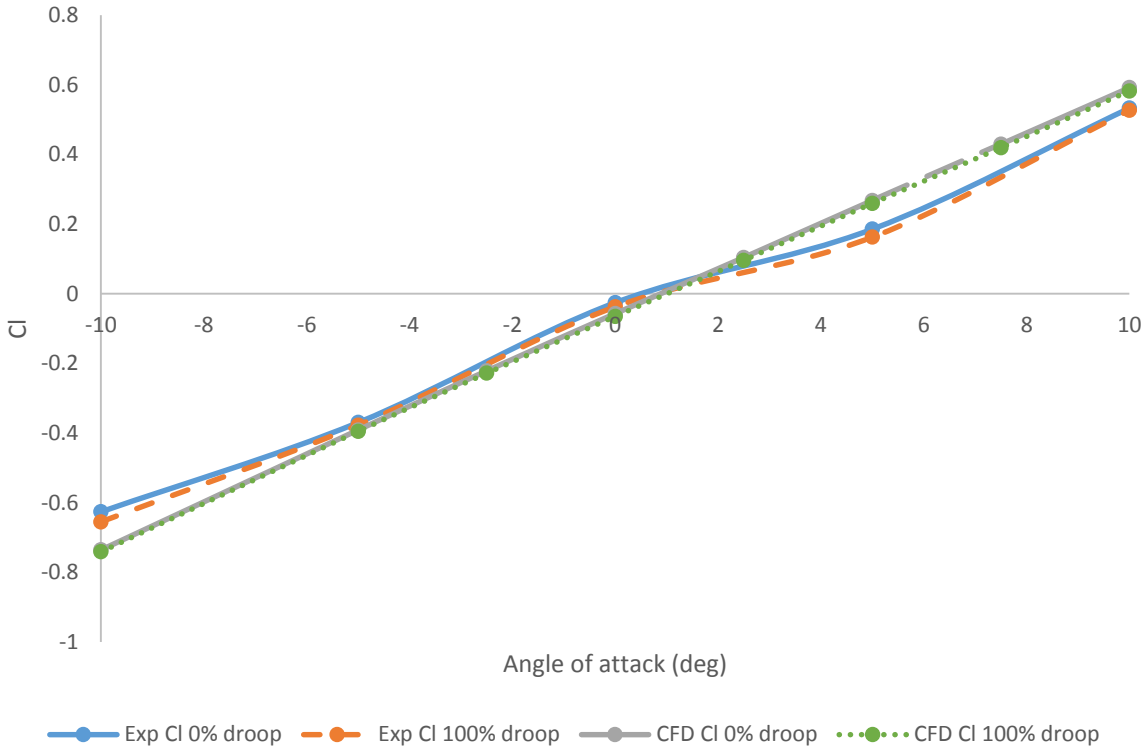

Figure 15 Comparison of experimental and CFD lift coefficients at 55m/s

7 CONCLUSIONS

Overall, the aims of the wind tunnel test were met and the proof-of-concept of the AMWT was demonstrated with the droop-nose device functioning successfully under aerodynamic loads. The test was unique amongst literature and much knowledge has been obtained by undertaking this test. The measured strain and pressure values had good agreement with the

FEA and CFD solutions, indicating that the skin and compliant mechanism performed well and as expected. The assembled droop nose matched closely to the target clean and droop surface shapes (when actuated), signifying that the design chain, with the constituent 3DSkinOpt and topology optimization tools, can lead to realisable morphing structures. A key finding from the tests was that the superelastic nickel titanium material has high suitability to morphing applications.

8 ACKNOWLEDGEMENTS

The presented work is carried out as part of the EU FP7 Project NOVEMOR Grant Agreement 285395 and the authors thank the European Commission for the research funding. Srinivas Vasista is a recipient of a Humboldt Postdoctoral Fellowship and is grateful for the financial support from the Alexander von Humboldt Foundation. The support of the Airbus Wind Tunnel Lab staff at Airbus Operations UK is also gratefully acknowledged.

9 COPYRIGHT STATEMENT

10 REFERENCES

[1] Report of the High Level Group on Aviation Research, “Flightpath 2050: Europe's Vision for Aviation,” European Commission, 2011.

[2] S. Barbarino, O. Bilgen, R. Ajaj, M. Friswell and D. Inman, ““A Review of Morphing Aircraft,” *Journal of Intelligent Material Systems and Structures,* vol. 1, January 2011.

[3] S. Vasista, H. P. Monner, A. de Gaspari and S. Ricci, “Morphing Devices for a Wing and Wingtip Based on Compliant Structures,” in *4th EASN Association International Workshop on Flight Physics and Aircraft Design*, Aachen, Germany, 2014.

[4] S. Vasista, J. Riemenschneider and H. P. Monner, “Design and Testing of a Compliant Mechanism-Based Demonstrator for a Droop-Nose Morphing Device,” in *SciTech Conference*, Kissimmee, Florida, United States, 2015.

[5] M. Kintscher, M. Wiedemann, H. P. Monner, O. Heintze and T. and Kühn, “Design of a Smart Leading Edge Device for Low Speed Wind Tunnel Tests in the European Project SADE,” *International Journal of Structural Integrity,* vol. 2, no. 4, pp. 383-405, 2011.

[6] J. Riemenschneider, S. Vasista, B. van de Kamp and H. P. Monner, “Bench Top Test of a Droop Nose with Compliant Mechanism,” in *ASME 2015 Conference on Smart Materials,*

Adaptive Structures and Intelligent Systems (SMASIS2015), Colorado Springs, September 21-23, 2015.

[7] T. Gerhold, O. Friedrich, J. Evans and M. Galle, "Calculation of complex three-dimensional configurations employing the DLR-TAU-code," in *AIAA paper 0167*, 1997.

[8] D. Keyes, A. Ecer, J. Periaux, N. Satofuka and P. Fox, "Parallel Computation of Turbulent Flows around Complex Geometries on Hybrid Grids with the DLR-TAU Code," in *In Parallel Computational Fluid Dynamics: Towards Teraflops, Optimization, and Novel Formulations: Proceedings of the Parallel CFD'99 Conference*, North-Holland, 2000.

[9] S. R. Allmaras, F. T. Johnson and P. R. Spalart, "Modifications and Clarifications for the Implementation of the Spalart-Allmaras Turbulence Model," in *ICCFD7-1902, 7th International Conference on Computational Fluid Dynamics*, Big Island, Hawaii, 2012.